

## Measurement of the $\pi^-p$ elastic scattering cross section near $180^\circ$ between 600 and 1280 MeV/c\*†

T. J. Richards,‡ D. G. Crabb,§ R. Keller,|| and J. R. O'Fallon

*Physics Department, Saint Louis University, Saint Louis, Missouri 63103*

R. J. Ott,\*\* J. Trischuk, and J. Va'vra††

*Physics Department, McGill University, Montreal, Canada*

L. S. Schroeder‡‡

*Institute for Atomic Research and Department of Physics, Iowa State University, Ames, Iowa 50010*

(Received 3 August 1973)

Differential cross sections for  $\pi^-p$  elastic scattering over the angular range  $155^\circ$  to  $177^\circ$  in the center-of-mass system have been measured at 33 incident pion momenta in the range 600 to 1280 MeV/c. The experiment, which was performed at the Bevatron at the Lawrence Berkeley Laboratory, employed a liquid hydrogen target, a double-arm spectrometer, and standard counter techniques to detect the elastic events. The data from this experiment are compared to all other published data in this momentum region. The over-all agreement is good. The data of this experiment are also compared with the results of the recent phase-shift analysis by Almehed and Lovelace. In the momentum region between 700 and 900 MeV/c, the slope of the backward angular distribution goes rapidly through zero from negative to positive, and the magnitude of the differential cross section falls by more than a factor of 10. Momentum-dependent structure is seen in the extrapolated differential cross sections at  $180^\circ$ . Two prominent dips in the  $180^\circ$  differential cross sections appear at 880 and 1150 MeV/c. This structure is discussed in terms of a direct-channel resonance model that assumes only resonant partial waves are contributing to the cross sections for large scattering angles.

### I. INTRODUCTION

Pion-nucleon scattering data in the momentum region under 3000 MeV/c have been phenomenologically classified in terms of resonances. In order to unfold the contributions of each resonance, total cross sections, differential cross sections over the entire angular range, polarization data, and spin-rotation parameters are needed. Large-angle differential cross sections are especially sensitive to resonant structure and put strong constraints on the masses of the resonances.

This experiment presents a systematic set of  $\pi^-p$  elastic differential cross sections at eight center-of-mass scattering angles from  $155^\circ$  to  $177^\circ$  for 33 values of incident-pion momenta in the range 600 to 1280 MeV/c. These measurements were made at the Lawrence Berkeley Laboratory (LBL) Bevatron. These data have been used in the recent phase-shift analysis of Almehed and Lovelace (CERN 71)<sup>1</sup> that determined a new set of resonance parameters. The results of the CERN 71 analysis and data from other recent experiments<sup>2-4</sup> will be compared with the data from this experiment.

A direct-channel resonance model which gives a reasonable fit to the  $180^\circ$  elastic cross sections will also be discussed.

### II. EXPERIMENTAL PROCEDURE

A double-arm spectrometer was employed to detect elastic scattering events and is shown in Fig. 1. The pion arm of the spectrometer consisted of an array of eight scintillation counters (A) and a gating counter (G). The proton arm of the spectrometer consisted of a dipole magnet for rough momentum analysis, a telescope of two 14-element arrays of scintillation counters (B, C), and a trigger counter (D). Elastic events were defined by requiring coincidences between the counters in the two arms. The incident beam was counted with scintillation counters (S) located upstream of the liquid hydrogen target.

#### A. Incident beam

Pions were obtained from an internal production target and transported to the liquid hydrogen target by the beam line shown in Fig. 1. The internal copper production target was  $0.635(T) \times 0.9525(W) \times 8.89(L)$  cm in size and scraped protons from the internal proton beam prior to its extraction. The first dipole "C" magnet,  $M_1$ , and the Bevatron main-ring magnets steered negatively charged particles out of the accelerator. Five quadrupole magnets,  $Q_1$  to  $Q_5$ , focused the particles into a spot at the center of the liquid hydrogen target.

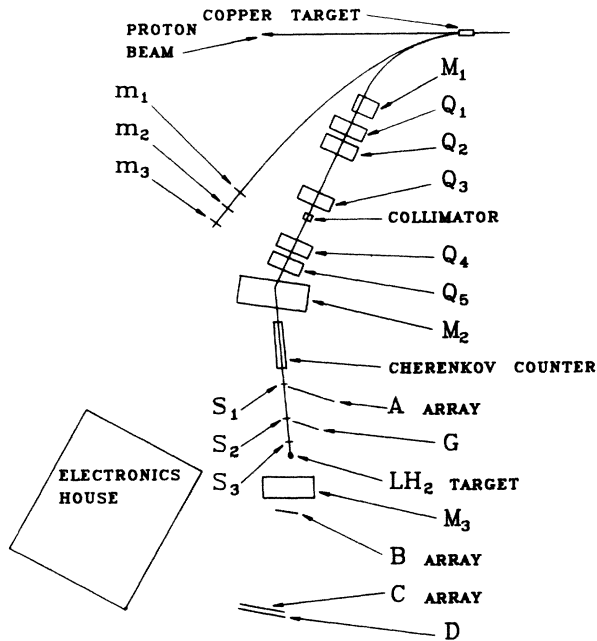


FIG. 1. Plan view of experimental layout. The  $M$ 's are dipole magnets, the  $Q$ 's are quadrupole magnets, and the  $m$ 's are scintillation counters that formed a monitor to view the internal Bevatron target. The beam line and monitor line are curved in the region near the copper target to represent the effect of the Bevatron magnets which are not shown. Incident pions were detected by scintillation counters labeled  $S$ . The scattered pions were detected by scintillation counters  $G$  and  $A$ , and recoil protons were detected by scintillation counters,  $B$ ,  $C$ , and  $D$ .

A second dipole "H" magnet,  $M_2$ , was located downstream of  $Q_5$  and defined the momentum of the incident pions. Current in  $M_2$  was regulated to within  $\pm\frac{1}{2}\%$ , which resulted in an uncertainty in the mean values of the incident momenta of approximately  $\pm\frac{1}{2}\%$ . A flip coil was used to measure the central-field values of  $M_2$  at each momentum point for which data were taken, and these measurements were in agreement with the original calibration measurements by the LBL Magnet Test Group.

Horizontal divergence in the beam, which depended on the width of the collimator located downstream of  $Q_3$  at the intermediate focus, was calculated with the computer program OPTIK.<sup>5</sup> To keep the horizontal beam divergence and the resulting momentum spread,  $\Delta p/p$ , within reasonable limits, the collimator opening was set at  $2.54 \times 2.54$  cm. This value gave a calculated beam divergence of  $\pm 15$  mrad horizontally and  $\pm 8$  mrad vertically, and a  $\Delta p/p$  of  $\pm 1.5\%$  at the hydrogen target.

In order to minimize multiple Coulomb scatter-

ing of the incident pions, helium bags were installed in the beam line. One helium bag covered the distance from the entrance of  $M_1$  to the exit of  $Q_3$ , and the second covered the distance from the intermediate focus to a point 2.65 m upstream from the center of the liquid hydrogen target. The beam intensity at the liquid hydrogen target increased by a factor of approximately 2 after the installation of the helium bags.

The 33 tabulated values of momenta at which data were taken corresponded to the momenta of incident pions at the center of the liquid hydrogen target. Due to a small energy loss of the incident pions in beam counters and gas between the exit of  $M_2$  and the target, corrections had to be made to the momentum values defined by  $M_2$ . These corrections amounted to less than 1% of the nominal  $M_2$  exit values over the entire range covered.

The lepton contamination in the beam was measured at every value of momentum with a gas threshold Cherenkov counter (pressure less than  $3 \text{ MN/m}^2$ ). Four gases, Freon 13, nitrogen, carbon dioxide, and sulfur hexafluoride, were used. At low momenta Freon 13 was used; however, the production of knock-on electrons in this dense gas gave a positive slope to the electron plateau which became more pronounced as the momentum was increased. In order to measure the true electron plateau, nitrogen was also used at the lower momenta. At higher momenta  $\text{CO}_2$  and  $\text{SF}_6$  were used. A typical Cherenkov pressure curve is shown in Fig. 2. Final lepton contaminations varied from  $(42 \pm 2)\%$  at  $600 \text{ MeV}/c$  to  $(8 \pm 2)\%$  at  $1280 \text{ MeV}/c$ . Figure 3 shows the measured averages of the percentage of pions in the beam as a function of incident momentum and the azimuthal position of the internal copper target used to generate the pions. The dips and bumps in Fig. 3 for a fixed azimuthal angle were due to the Bevatron magnets and the first magnet in the beam line,  $M_1$ . The current in  $M_1$  was changed for each new value of momentum and consequently changed the pion production angle accepted by the rest of the beam magnets.

The beam was retuned for each value of incident beam momentum. A monitor telescope viewed the internal target, and tuning consisted of maximizing the beam intensity at the center of the liquid hydrogen target relative to the coincidence rate in this monitor. The variable parameters for tuning the beam were the radial and azimuthal positions of the internal target and the currents in magnets  $M_1$  and  $Q_1$ - $Q_5$ . Typical beam rates were  $5 \times 10^5$  particles per pulse entering the liquid hydrogen target for  $5 \times 10^{11}$  protons hitting the internal copper target. The proton spill length was approximately one second with a Bevatron rate of ten

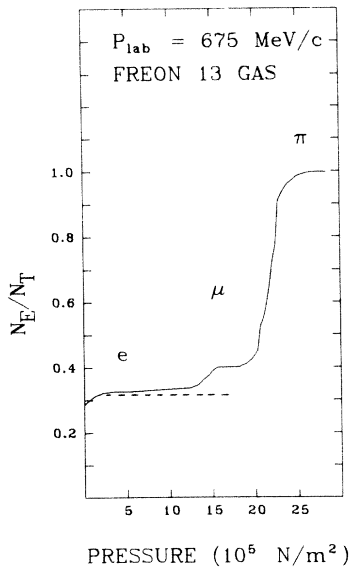


FIG. 2. Example of a Cherenkov curve used to measure beam contamination at low momentum. The ratio  $N_E/N_T$  is the number of coincidences among the Cherenkov counter and two scintillation counters placed at the entrance and exit of the Cherenkov counter divided by the number of coincidences between the scintillation counters. The solid curve was obtained using Freon 13. Knock-on electrons in Freon 13 caused the electron plateau to rise with increasing gas pressure. In order to measure the true electron plateau, nitrogen was also used and gave the dashed curve.

pulses per minute.

Spatial distributions of the beam were determined for the best tune values at all momenta. A hodoscope was placed at the location of the liquid hydrogen target and measured the vertical and horizontal particle distributions simultaneously.

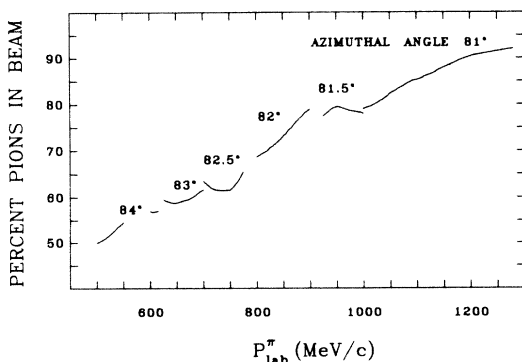


FIG. 3. Percent pions in incident beam as a function of incident pion momenta and azimuthal positions of the internal Bevatron target.

These distributions were found to be Gaussian in shape with full widths of typically 2.6 cm.

### B. Liquid hydrogen target

The liquid hydrogen target consisted of a cylindrical flask with an effective length of  $21.11 \pm 0.08$  cm. The flask walls consisted of  $12.7 \mu\text{m}$  Mylar surrounded by ten wraps of  $6.35\text{-}\mu\text{m}$  aluminized Mylar. A two-window vacuum jacket surrounded this flask. The window for the scattered pions was made of  $762\text{-}\mu\text{m}$  Mylar, while the smaller window for the recoil protons was  $508\text{-}\mu\text{m}$  Mylar. The flask was connected to a 10-liter reservoir of liquid hydrogen.

### C. Spectrometer

The backward-scattered pions were detected by a single gating counter,  $G$ , in coincidence with an array of scintillation counters, the  $A$  array. The recoil protons were momentum-analyzed by the dipole magnet,  $M_3$ , and were detected by the  $B$ ,  $C$ , and  $D$  scintillation counters.

The  $A$  array, consisting of eight close-packed scintillation counters each with dimensions  $71.12(L) \times 25.4(W) \times 1.27(T)$  cm, defined the laboratory angular bins that are listed in Table I. These angular bins gave the desired resolution in the cosine of the scattered pion angles. The  $A$  array was positioned such that a reasonably long time of flight from the liquid hydrogen target to the  $A$  array for the scattered pion ( $\beta \approx 1$ ) was obtained in order to have timing information available to aid in rejecting inelastic events. In addition, the beam-axis edge of  $A_1$  had to be far enough away from the beam so that the singles rate in  $A_1$  due to spray from the beam was kept to a tolerable level. The near edge of  $A_1$  was placed on a  $3^\circ$  line with respect to the beam axis a distance of 3.21 m from the center of the liquid hydrogen target.

TABLE I. Laboratory angular bins for scattered pions. Near edge refers to the edge of the counter nearest the incident beam.

A-counter number	Cosine of near edge	Cosine of center	Cosine resolution
1	-0.9986	-0.9961	0.0065
2	-0.9921	-0.9866	0.0128
3	-0.9793	-0.9703	0.0199
4	-0.9594	-0.9467	0.0274
5	-0.9320	-0.9154	0.0352
6	-0.8968	-0.8765	0.0423
7	-0.8545	-0.8308	0.0487
8	-0.8058	-0.7795	0.0536

This kept the  $A$  singles rates low enough that the accidental AGS coincidence rate (to be defined in the section on logic, Sec. II D) was acceptable.

The gating counter,  $G$ , which had the shape of a symmetric trapezoid, defined the vertical acceptance of the detection system. It had dimensions  $5.84(L_1) \times 11.68(L_2) \times 50.80(W) \times 0.634(T)$  cm and was located 61 cm from the center of the liquid hydrogen target. Kinematic calculations for  $\pi^-p$  elastic scattering projected the shape of the  $G$  counter onto the  $A$  array and determined the minimum vertical length of the  $A$  counters needed to accept elastically scattered pions.

Magnet  $M_3$  was positioned and its current set so that the incident beam bent  $10^\circ$  in order to miss the  $B$ ,  $C$ , and  $D$  counters and also so that the recoil protons traveled through the central portion of  $M_3$ , where the magnetic field was most uniform.

The  $B$  array consisted of 14 close-packed scintillation counters with dimensions  $25.4(L) \times 5.08(W) \times 0.635(T)$  cm. The dimensions and positions of this array were specified by the requirements of good proton angular resolution and uniform time of flight for protons from the target to each  $B$  counter. At least three  $B$  counters were required to detect recoil protons which corresponded to pions hitting a single  $A$  counter. This requirement determined the width of the individual  $B$  counters. Elastic events were, therefore, detected in more than one proton angular bin, and any anomalous structure in the proton distributions was readily visible. In addition, several extra angular bins were available outside of the elastic peak in order to estimate the shape of the background.

The  $C$  array also consisted of 14 close-packed

scintillation counters with dimensions  $66.04(L) \times 25.4(W) \times 1.27(T)$  cm. The even-numbered  $C$  counters were positioned in back of the odd-numbered counters in one-to-one correspondence with the  $B$  array to produce a 14-element telescope. The  $C$  array provided time-of-flight information in addition to providing a constraint on the momentum resolution of the proton arm of the spectrometer. The  $C$  counters overmatched the  $B$  counters to allow for multiple Coulomb scattering of protons in air and in the  $B$  array.

The  $D$  counter consisted of a single scintillator with dimensions  $182.88(W) \times 68.0(L) \times 1.27(T)$  cm and was viewed by four photomultipliers. Pulses from this counter formed a part of the strobe signal triggered by recoil protons. The strobe signal is described in the section on logic.

#### D. Logic

The electronic logic was designed so that all eight differential cross sections could be measured and monitored simultaneously. The positions of the counters remained fixed for all momenta, and once the incident beam was tuned for a given value of momentum, data taking was continuous.

The logic was divided into two parts. The first part was the formation of a strobe triggered by elastic events which strobed the  $A$ ,  $B$ , and  $C$  arrays in fast coincidence (resolution 20–30 nsec). The second part consisted of event storage in which the elastic events were encoded and stored in an eight-by-fourteen-address matrix that denoted which  $A$  counter and  $BC$  pair of counters had fired. Both parts of the logic are schematically illustrated in Fig. 4.

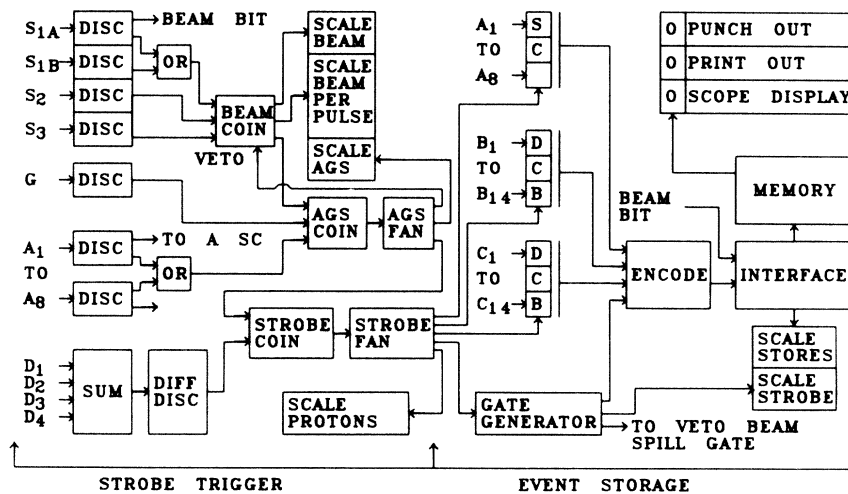


FIG. 4. Electronic logic used to form the strobe trigger and to store the elastic events. Key: DISC—discriminator, COIN—coincidence, FAN—fanout, DIFF DISC—differential discriminator, DCB—discriminator and coincidence and buffer, SC—strobed coincidence.

Figure 4 shows the strobe trigger which consisted essentially of a fourfold coincidence between (i)  $S$ , a beam coincidence pulse, (ii)  $G$ , a pulse from the gating counter, (iii)  $A$ , a pulse from any of the eight pion counters, and (iv)  $D$ , a pulse which was the sum of pulses from the four  $D$  phototubes. If there was only a single  $A$  pulse, and if a matching pair of  $B$  and  $C$  counter pulses were in coincidence with the strobe pulse, then an elastic event was recorded.

The ND 2200 analyzer required 30  $\mu$ sec to process an event, and while an event was being processed and stored beam coincidences were gated off. For the maximum beam rate of approximately 500 000 particles per Bevatron pulse, the strobe rates were never greater than 100 per Bevatron pulse, which resulted in a maximum system dead time of less than 1%.

Beam counters  $S_{1A}$  and  $S_{1B}$  were positioned side by side in the beam with their common boundary passing through the nominal beam center. Events due to pions going through  $S_{1A}$  were stored separately in the analyzer memory from events due to pions going through  $S_{1B}$ . The pulse labeled "beam bit" was used for this event separation. Event separation was done in order to see if the width of the liquid hydrogen target and the profile of the incident pion beam would produce differences in the widths and shapes of the proton distributions across the  $B$  and  $C$  counter arrays. No differences were seen in the two sets of proton distributions, and these distributions were added together for final analysis.

Counters  $S_{1A}$  and  $S_{1B}$  also provided a crude monitor of beam position since relative changes in their counting rates indicated that the beam was no longer centered between them.

The encoder and interface modules that directly addressed the memory of the ND 2200 analyzer were constructed specifically for this experiment. All other modules were obtained commercially or from the LBL electronic equipment pool.

### III. DATA ANALYSIS

Eight differential cross sections were measured simultaneously at each of 33 values of incident-pion momenta. The angular dependence was defined by the position of the eight  $A$  counters with respect to the center of the liquid hydrogen target and incident beam axis. The formula used to calculate differential cross sections for given values of incident-pion momentum and scattering angle was

$$\frac{d\sigma}{d\Omega_{c.m.}} = \frac{N_e X}{N_\pi N_p \Delta\Omega_{c.m.}}, \quad (3.1)$$

where  $N_e$  is the number of elastic  $\pi^-p$  events;  $N_\pi$  is the number of incident pions;  $N_p$  is the number of protons in the liquid hydrogen target per unit area;  $\Delta\Omega_{c.m.}$  is the corresponding center-of-mass solid angle; and  $X$  is the over-all correction factor and is equal to the product of  $X^a$ , the correction factor due to particle absorption, and  $X^{dk}$ , the correction factor due to scattered pion decay.

The formula used to calculate  $N_p$  was

$$N_p = \frac{\rho L n_0}{A}, \quad (3.2)$$

where  $\rho$  is the density of liquid hydrogen ( $\text{g}/\text{cm}^3$ ),  $L$  is the effective length of the target flask (cm),  $n_0$  is Avogadro's number ( $\text{mole}^{-1}$ ), and  $A$  is the atomic number of hydrogen ( $\text{g}/\text{mole}$ ).

The liquid hydrogen in the target flask was in thermal equilibrium with a reservoir that was filled with liquid hydrogen. The pressure inside the reservoir was monitored before and after each data run. Fluctuations in these pressure readings gave rise to an uncertainty in  $\rho$  of  $\pm 1\%$ . The value of  $\rho$  was determined to be  $0.0708 \pm 0.0007 \text{ g}/\text{cm}^3$ .<sup>6</sup> With an effective flask length for all incident pions of  $21.11 \pm 0.08 \text{ cm}$ , Eq. (3.2) gives a value for  $N_p$  of  $(8.93 \pm 0.09) \times 10^{23} \text{ protons}/\text{cm}^2$ .

The measurement of  $N_\pi$  was described in Sec. II. These values give an estimated percent uncertainty in the number of incident pions of  $\pm 3.5\%$ .

The center-of-mass solid angle for each angular bin was calculated numerically using a Monte Carlo computer program. This program took into account incident beam divergence and beam shape, finite dimensions of the hydrogen target, energy loss, and multiple Coulomb scattering of scattered and recoil particles in air, liquid hydrogen target, and scintillation counters. The Monte Carlo program generated more than 2500 events into each of the eight angular bins at 600, 800, 1000, 1200, and 1280 MeV/c. The smoothly varying solid angles were then fitted with a quadratic function in  $\cos\theta_{c.m.}^\pi$  and incident momentum, and interpolations were made to determine the solid angles at each of the 33 values of incident pion momenta where differential cross sections were measured. The solid angles varied from 1.7 msr to 6.2 msr. The final uncertainties in the interpolated solid angles, which were determined from the quadratic fits to the Monte Carlo values and estimates of the over-all accuracy of the program, were  $\pm 2\%$ . Solid angles determined in this way had systematic differences of not more than 3% with the results of a simplified numerical integration (not Monte Carlo) which was done at each momentum.

In order to determine the number of elastic events, the total event spectra across the  $BC$  arrays were considered. An example of a total

event spectrum is shown in Fig. 5. In this figure there are eight angular distributions of the recoil protons displayed in histogram form. Each histogram corresponds to one *A* counter and has 14 angular bins; one angular bin for each matched pair of *BC* counters. These distributions are assumed to be the sum of three separate distributions.

The first of these individual distributions was due to elastic events. The elastic event distribution had a sharp peak with a full width at half-maximum of two to three *BC* channels. The location and the full width at half-maximum agreed with predictions from the Monte Carlo program. An example of these predictions is shown in Fig. 6.

The second distribution arises from  $\pi^+p$  interactions in the target walls, windows, and beam counters. This distribution was measured by taking data with no liquid hydrogen in the flask. An example of a target-empty distribution is shown in Fig. 7. In this figure there are again eight histograms representing the recoil-proton angular distributions across the *BC* counter arrays. One can see that these histograms have small peaks in the same channels as the elastic peaks which look like elastic events. The number of target-empty events that had to be subtracted varied from 2% to 6% of the original total number of events.

The third distribution was smooth over the entire

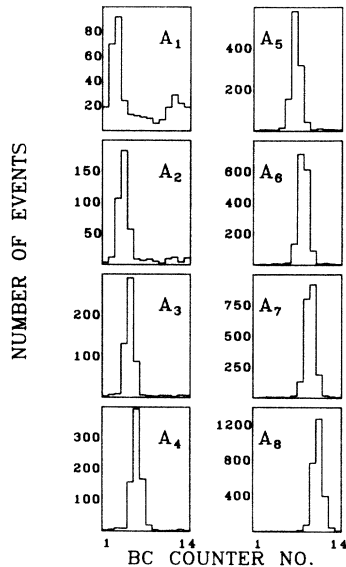


FIG. 5. Examples of target-full proton angular distributions across the *BC* counter arrays. The distributions are displayed in histogram form; each 14-channel histogram corresponds to one of the eight *A* counters. Incident pion momentum is 1000 MeV/*c*, and the total incident beam is  $5 \times 10^8$  particles.

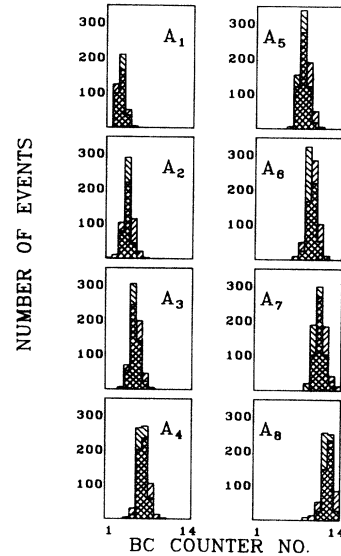


FIG. 6. Proton angular distributions across the *BC* counter arrays compared to the predictions of the Monte Carlo calculations. The number of elastic events generated by the Monte Carlo program was normalized to the number of data events in the elastic *BC* channels. The positive-slope lines, ///, correspond to data events, and the negative-slope lines, \\, correspond to Monte Carlo events. The incident momentum is 600 MeV/*c*, and the total incident beam is  $2 \times 10^8$  particles.

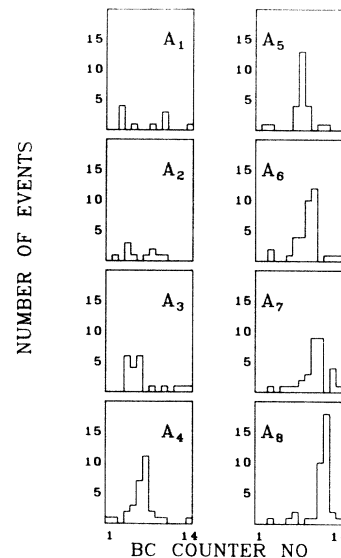


FIG. 7. Examples of target-empty proton angular distributions across the *BC* counter arrays. The distributions are displayed in histogram form; each 14-channel histogram corresponds to one of the eight *A* counters. The incident momentum is 1000 MeV/*c*, and the total incident beam is  $3 \times 10^8$  particles.

$BC$  counter arrays and was assumed to be due to inelastic events. In order to be convinced that inelastic events should form a smooth flat background, the  $n$ -body final-state Monte Carlo computer program, FOWL,<sup>7</sup> was used to generate events from single-pion and  $\rho$ -production-type interactions. These computer-generated events were put into angular bins defined by the geometry of this counter system and plotted out in the same histogram form used to collect the elastic data. All computer-generated histograms were smooth across the 14  $BC$  channels. These investigations showed that only  $\pi^-p$  elastic events were likely to produce such a narrow peak in the proton distribution.

A smooth curve was drawn through the low flat part of the histograms, and these background events were subtracted from the elastic peak. The smooth background varied from 2% to 8%. The subtracted smooth background and target-empty events had uncertainties of less than 10%, giving rise to an additional statistical uncertainty in the number of elastic events of less than 1%.

During the experiment equipment failures resulted in inefficiencies in a few  $BC$  channels in some of the data runs. Normalization of those  $BC$  channels with inefficiencies was accomplished by using data runs with no inefficiencies to calculate correction factors. Complete explanations of these correction factors are given in Ref. 8. Less than 12% of the data was affected, and good data runs were always available for comparison.

Because of pion and proton absorption and scattering in air, liquid hydrogen, target walls and windows, and in the plastic  $G$ ,  $B$ , and  $C$  counters, a small percentage of elastic events were not counted. Cross-section data for pions and protons in carbon and hydrogen were used to calculate the particle absorption.<sup>9-19</sup> The plastic scintillation counters and the Mylar windows and walls of the target were approximated by relative percentages of carbon, hydrogen, and oxygen. The correction factor due to absorption,  $X^a$ , was calculated using

$$X^a = \exp \left( \sum_{i=1}^m N_i L_i \sigma_i \right), \quad (3.3)$$

where  $i$  is the index denoting a particular absorption process, e.g., a pion being absorbed by liquid hydrogen;  $m = 11$ , the number of absorption and scattering interactions of pion and protons in various materials;  $N_i$  is the number of absorbing and/or scattering nuclei per unit volume ( $\text{cm}^{-3}$ );  $\sigma_i$  is the cross section for a particle to be absorbed or scattered out of the counter system ( $\text{cm}^2$ ); and  $L_i$  is the distance a particle travels through material  $i$ . At each momentum this cal-

ulation was done for all scattering angles. The values of  $N_i$  and  $L_i$  were determined to within a few percent by knowing the size and composition of the counter system. The total uncertainty in the value of the sum in the exponent of Eq. (3.3) was estimated to be  $\pm 20\%$ . Since the value of this sum was small, the resulting uncertainty in  $X^a$  was only  $\pm 2\%$ . Values of  $X^a$  ranged from a minimum of 1.088 at 1280 MeV/ $c$  to a maximum of 1.122 at 600 MeV/ $c$ .

The pion decay correction was calculated using a Monte Carlo computer program. Events were generated for back-scattered pions that decayed with the correct rest-frame lifetime and corresponded to recoil protons that were detected by the  $B$  and  $C$  arrays. The muon was created isotropically in the rest frame of the pion and tracked in the lab frame to see if it hit an  $A$  counter or, for early decays, if it made a  $G \cdot A_i$  coincidence. The decay correction factor was calculated using

$$X_i^{dk} = N_i^\pi / [N_i^\pi - N_i^\mu(\text{out}) + N_i^\mu(\text{in})], \quad (3.4)$$

where  $i$  is the index for a particular  $A$  counter,  $N_i^\pi$  is the number of computer-generated pions making a  $G \cdot A_i$  hit,  $N_i^\mu(\text{out})$  is the number of muons from computer-generated decays of  $N_i^\pi$  that do not make a  $G \cdot A_i$  hit, and  $N_i^\mu(\text{in})$  is the number of muons from computer-generated decays of  $N_{j \neq i}^\mu$  that do make a  $G \cdot A_i$  hit. The above calculation assumes that recoil protons corresponding to decay muons are not detected outside of the neighboring  $A$  counter's elastic peak. This assumption is valid because the proton distributions for two adjacent  $A$  counters overlap each other. The angular distribution across counter boundaries was assumed uniform in these calculations. This approximation introduced negligible errors because  $N_i^\mu(\text{in})$  and  $N_i^\mu(\text{out})$  comprised at most  $\approx 4\%$  of the scattered pions. The decay correction factor was small and ranged from a maximum of 1.03 at 600 MeV/ $c$  to a minimum of 1.00 at 1280 MeV/ $c$ . These values all had an uncertainty of  $\pm 2\%$  due to the finite number of events generated and the interpolation used to calculate values other than those for which the Monte Carlo program was run.

A complete listing of all cross sections is given in Table II. The statistical uncertainty in the cross sections was due only to  $\Delta N_e$ , the uncertainty in the number of elastic events, and typically ranged from 3% to 10%. The uncertainties in  $X$ ,  $N_\pi$ ,  $N_p$ , and  $\Delta \Omega_{\text{c.m.}}$  were added in quadrature to give an over-all systematic uncertainty of approximately  $\pm 5\%$ .

TABLE II.  $\pi^-p$  elastic differential cross sections in the center-of-mass system.

$P_{\text{lab}}^a$ (MeV/c)	$E_{\text{c.m.}}^b$ (MeV)	$-\cos\theta_{\text{c.m.}}$	$d\sigma/d\Omega$ (mb/sr)	$u$ [(GeV/c) $^2$ ]	$d\sigma/du$ [mb/(GeV/c) $^2$ ]	Error $^c$ (%)
600	1434	0.9984	1.279	0.360	26.06	6
		0.9945	1.265	0.359	25.78	5
		0.9877	1.347	0.357	27.46	5
		0.9778	1.309	0.354	26.68	4
		0.9644	1.249	0.349	25.45	4
		0.9474	1.210	0.344	24.67	4
		0.9268	1.132	0.338	23.06	4
		0.9030	1.023	0.331	20.85	4
614	1443	0.9984	1.127	0.356	22.21	7
		0.9945	1.511	0.354	29.77	5
		0.9879	1.312	0.352	25.85	5
		0.9781	1.295	0.349	25.52	5
		0.9648	1.403	0.345	27.64	5
		0.9480	1.292	0.339	25.46	5
		0.9277	1.327	0.333	26.15	4
		0.9041	1.028	0.325	20.25	5
625	1450	0.9984	1.457	0.352	27.97	3
		0.9946	1.469	0.351	28.21	3
		0.9880	1.309	0.349	25.13	3
		0.9783	1.411	0.346	27.09	3
		0.9651	1.219	0.341	23.40	3
		0.9485	1.266	0.336	24.31	3
		0.9284	1.091	0.329	20.95	3
		0.9050	1.023	0.322	19.64	3
658	1470	0.9985	1.379	0.342	24.57	4
		0.9947	1.460	0.341	26.02	4
		0.9883	1.615	0.339	28.79	3
		0.9789	1.601	0.335	28.53	3
		0.9661	1.370	0.331	24.42	3
		0.9499	1.347	0.325	24.00	3
		0.9303	1.217	0.318	21.69	3
		0.9075	1.168	0.310	20.81	3
675	1481	0.9985	1.629	0.337	27.99	5
		0.9948	1.662	0.336	28.54	4
		0.9885	1.640	0.334	28.17	4
		0.9792	1.662	0.330	28.54	4
		0.9666	1.561	0.326	26.81	4
		0.9506	1.585	0.320	27.23	4
		0.9313	1.410	0.313	24.22	4
		0.9088	1.376	0.305	23.64	4
707	1501	0.9985	1.666	0.328	26.78	3
		0.9950	1.712	0.327	27.52	3
		0.9888	1.634	0.325	26.27	3
		0.9797	1.602	0.321	25.76	3
		0.9674	1.548	0.316	24.88	2
		0.9519	1.504	0.310	24.18	2
		0.9330	1.419	0.303	22.81	2
		0.9111	1.281	0.294	20.60	2
726	1512	0.9986	1.497	0.323	23.17	3
		0.9950	1.485	0.322	22.99	3
		0.9890	1.458	0.320	22.58	3
		0.9800	1.511	0.316	23.40	3
		0.9679	1.432	0.311	22.18	3
		0.9526	1.370	0.305	21.21	3
		0.9340	1.295	0.297	20.05	3
		0.9124	1.243	0.288	19.25	3

TABLE II. (Continued)

$P_{\text{lab}}^a$ (MeV/c)	$E_{\text{c.m.}}^b$ (MeV)	$-\cos\theta_{\text{c.m.}}$	$d\sigma/d\Omega$ (mb/sr)	$u$ [(GeV/c) <sup>2</sup> ]	$d\sigma/du$ [mb/(GeV/c) <sup>2</sup> ]	Error <sup>c</sup> (%)
750	1527	0.9986	1.175	0.317	17.37	3
		0.9951	1.140	0.316	16.87	3
		0.9892	1.093	0.313	16.17	3
		0.9804	1.096	0.310	16.21	3
		0.9685	1.077	0.304	15.94	3
		0.9535	1.065	0.298	15.75	2
		0.9352	1.025	0.290	15.16	2
		0.9140	1.013	0.281	14.99	2
777	1543	0.9986	0.793	0.311	11.16	4
		0.9952	0.840	0.309	11.82	4
		0.9894	0.791	0.306	11.13	3
		0.9808	0.784	0.303	11.04	3
		0.9692	0.845	0.297	11.90	3
		0.9544	0.848	0.291	11.93	3
		0.9365	0.863	0.283	12.15	3
		0.9157	0.850	0.274	11.96	3
800	1557	0.9986	0.451	0.305	6.10	5
		0.9953	0.511	0.304	6.90	4
		0.9896	0.500	0.301	6.76	4
		0.9811	0.554	0.297	7.48	3
		0.9697	0.564	0.292	7.62	3
		0.9552	0.617	0.285	8.34	3
		0.9376	0.633	0.277	8.56	3
		0.9171	0.685	0.267	9.25	3
825	1572	0.9987	0.303	0.299	3.93	6
		0.9954	0.303	0.298	3.92	5
		0.9898	0.342	0.295	4.42	5
		0.9815	0.381	0.291	4.94	4
		0.9703	0.438	0.286	5.67	4
		0.9560	0.544	0.279	7.04	3
		0.9387	0.556	0.270	7.19	3
		0.9186	0.619	0.261	8.02	3
850	1586	0.9987	0.213	0.294	2.64	7
		0.9955	0.228	0.292	2.83	6
		0.9900	0.265	0.289	3.30	6
		0.9818	0.328	0.285	4.08	5
		0.9708	0.397	0.280	4.94	4
		0.9568	0.492	0.273	6.11	3
		0.9398	0.568	0.264	7.05	3
		0.9200	0.663	0.254	8.23	3
875	1601	0.9987	0.139	0.289	1.66	10
		0.9956	0.175	0.287	2.09	8
		0.9901	0.191	0.284	2.28	7
		0.9821	0.282	0.280	3.37	5
		0.9713	0.374	0.274	4.46	4
		0.9576	0.477	0.267	5.70	3
		0.9409	0.562	0.258	6.71	3
		0.9214	0.737	0.248	8.80	2
900	1615	0.9987	0.123	0.283	1.42	11
		0.9956	0.176	0.282	2.02	8
		0.9903	0.247	0.279	2.84	5
		0.9825	0.322	0.274	3.70	4
		0.9718	0.442	0.269	5.08	4
		0.9583	0.552	0.261	6.35	3
		0.9419	0.719	0.252	8.26	3
		0.9228	0.839	0.242	9.64	2

TABLE II. (*Continued*)

$P_{\text{lab}}^a$ (MeV/c)	$E_{\text{c.m.}}^b$ (MeV)	$-\cos\theta_{\text{c.m.}}$	$d\sigma/d\Omega$ (mb/sr)	$u$ [(GeV/c) <sup>2</sup> ]	$d\sigma/du$ [mb/(GeV/c) <sup>2</sup> ]	Error <sup>c</sup> (%)
925	1629	0.9988	0.155	0.278	1.72	9
		0.9957	0.193	0.277	2.14	8
		0.9905	0.232	0.274	2.57	6
		0.9828	0.357	0.269	3.95	4
		0.9723	0.471	0.263	5.22	4
		0.9590	0.641	0.256	7.10	3
		0.9429	0.750	0.247	8.30	3
		0.9241	1.056	0.236	11.69	2
950	1644	0.9988	0.187	0.274	2.00	7
		0.9958	0.243	0.272	2.59	5
		0.9906	0.338	0.269	3.61	4
		0.9831	0.442	0.264	4.72	3
		0.9728	0.609	0.258	6.51	3
		0.9597	0.821	0.251	8.77	2
		0.9438	0.993	0.241	10.61	2
		0.9253	1.145	0.230	12.23	2
965	1652	0.9988	0.288	0.271	3.01	5
		0.9958	0.324	0.269	3.39	4
		0.9907	0.382	0.266	4.00	4
		0.9832	0.529	0.261	5.53	3
		0.9731	0.707	0.255	7.40	2
		0.9601	0.934	0.248	9.77	2
		0.9444	1.146	0.238	11.99	2
		0.9260	1.400	0.227	14.65	2
975	1658	0.9988	0.230	0.269	2.37	9
		0.9959	0.294	0.267	3.03	7
		0.9908	0.390	0.264	4.02	6
		0.9833	0.497	0.259	5.13	5
		0.9732	0.726	0.253	7.49	4
		0.9604	0.930	0.246	9.59	3
		0.9448	1.211	0.236	12.50	3
		0.9265	1.502	0.225	15.50	2
990	1666	0.9988	0.219	0.266	2.22	9
		0.9959	0.346	0.264	3.49	6
		0.9909	0.409	0.261	4.13	5
		0.9835	0.583	0.257	5.89	4
		0.9735	0.771	0.250	7.79	4
		0.9608	1.044	0.243	10.55	3
		0.9453	1.321	0.233	13.35	3
		0.9272	1.562	0.222	15.78	2
1000	1672	0.9988	0.278	0.264	2.78	5
		0.9959	0.363	0.263	3.62	4
		0.9910	0.455	0.260	4.53	4
		0.9836	0.601	0.255	6.00	3
		0.9737	0.821	0.249	8.19	2
		0.9610	1.075	0.241	10.72	2
		0.9456	1.346	0.231	13.42	2
		0.9277	1.625	0.220	16.21	2
1015	1680	0.9988	0.306	0.262	2.99	9
		0.9960	0.373	0.260	3.64	7
		0.9910	0.445	0.257	4.35	6
		0.9838	0.630	0.252	6.16	5
		0.9739	0.862	0.246	8.42	4
		0.9614	1.109	0.238	10.84	3
		0.9462	1.413	0.228	13.81	3
		0.9284	1.652	0.217	16.16	3

TABLE II. (Continued)

$P_{\text{lab}}^a$ (MeV/c)	$E_{\text{c.m.}}^b$ (MeV)	$-\cos\theta_{\text{c.m.}}$	$d\sigma/d\Omega$ (mb/sr)	$u$ [(GeV/c) <sup>2</sup> ]	$d\sigma/du$ [mb/(GeV/c) <sup>2</sup> ]	Error <sup>c</sup> (%)
1030	1688	0.9988	0.298	0.259	2.85	7
		0.9960	0.404	0.257	3.87	5
		0.9911	0.473	0.254	4.53	4
		0.9839	0.647	0.249	6.21	3
		0.9742	0.862	0.243	8.26	3
		0.9618	1.078	0.235	10.33	2
		0.9467	1.365	0.225	13.09	2
		0.9291	1.623	0.214	15.56	2
1055	1702	0.9989	0.222	0.255	2.06	13
		0.9961	0.338	0.253	3.14	7
		0.9913	0.450	0.250	4.18	4
		0.9842	0.561	0.245	5.21	4
		0.9746	0.789	0.239	7.33	3
		0.9624	1.022	0.230	9.50	3
		0.9475	1.282	0.220	11.91	2
		0.9302	1.506	0.209	13.98	2
1085	1718	0.9989	0.210	0.250	1.88	9
		0.9961	0.285	0.248	2.55	6
		0.9914	0.343	0.245	3.07	6
		0.9845	0.485	0.240	4.34	4
		0.9751	0.659	0.234	5.90	4
		0.9631	0.881	0.225	7.89	3
		0.9485	1.096	0.215	9.81	2
		0.9314	1.331	0.203	11.91	2
1100	1726	0.9989	0.144	0.248	1.26	11
		0.9962	0.216	0.246	1.90	7
		0.9915	0.257	0.243	2.26	6
		0.9846	0.394	0.238	3.46	5
		0.9753	0.550	0.231	4.84	3
		0.9634	0.730	0.222	6.42	3
		0.9490	0.930	0.212	8.18	3
		0.9321	1.130	0.200	9.93	2
1121	1738	0.9989	0.099	0.245	0.85	12
		0.9962	0.138	0.243	1.18	8
		0.9916	0.216	0.239	1.85	5
		0.9848	0.300	0.234	2.58	4
		0.9756	0.438	0.228	3.75	3
		0.9639	0.589	0.219	5.05	2
		0.9496	0.760	0.208	6.52	2
		0.9329	0.929	0.196	7.97	2
1150	1753	0.9989	0.052	0.240	0.43	23
		0.9963	0.101	0.238	0.84	11
		0.9918	0.157	0.235	1.30	7
		0.9851	0.224	0.230	1.86	5
		0.9760	0.345	0.223	2.86	4
		0.9645	0.485	0.214	4.02	3
		0.9505	0.603	0.204	5.00	2
		0.9340	0.736	0.191	6.11	2
1180	1769	0.9989	0.102	0.236	0.82	14
		0.9964	0.130	0.234	1.04	10
		0.9919	0.161	0.230	1.29	8
		0.9854	0.216	0.225	1.73	6
		0.9765	0.276	0.218	2.22	5
		0.9651	0.400	0.209	3.21	4
		0.9513	0.485	0.199	3.89	3
		0.9352	0.594	0.186	4.77	3

TABLE II. (Continued)

$P_{\text{lab}}^a$ (MeV/c)	$E_{\text{c.m.}}^b$ (MeV)	$-\cos\theta_{\text{c.m.}}$	$d\sigma/d\Omega$ (mb/sr)	$u$ [(GeV/c) <sup>2</sup> ]	$d\sigma/du$ [mb/(GeV/c) <sup>2</sup> ]	Error <sup>c</sup> (%)
1200	1780	0.9990	0.110	0.233	0.86	12
		0.9964	0.125	0.231	0.98	9
		0.9920	0.160	0.228	1.26	7
		0.9855	0.197	0.222	1.55	5
		0.9767	0.289	0.215	2.27	4
		0.9655	0.361	0.206	2.83	3
		0.9519	0.437	0.195	3.43	3
		0.9359	0.562	0.183	4.41	3
1210	1785	0.9990	0.176	0.232	1.37	9
		0.9964	0.161	0.230	1.25	8
		0.9921	0.183	0.226	1.42	7
		0.9856	0.231	0.221	1.80	5
		0.9769	0.272	0.214	2.11	4
		0.9657	0.367	0.205	2.85	4
		0.9522	0.435	0.194	3.38	3
		0.9363	0.510	0.181	3.96	3
1230	1795	0.9990	0.151	0.229	1.14	10
		0.9965	0.166	0.227	1.26	8
		0.9922	0.177	0.223	1.35	8
		0.9858	0.229	0.218	1.74	6
		0.9771	0.272	0.211	2.07	5
		0.9661	0.358	0.202	2.72	4
		0.9527	0.421	0.191	3.20	4
		0.9370	0.493	0.178	3.75	4
1250	1806	0.9990	0.186	0.226	1.39	9
		0.9965	0.194	0.224	1.44	7
		0.9922	0.219	0.221	1.63	6
		0.9859	0.247	0.215	1.84	6
		0.9774	0.296	0.208	2.21	5
		0.9665	0.336	0.199	2.50	5
		0.9532	0.419	0.188	3.12	4
		0.9377	0.502	0.175	3.74	4
1280	1821	0.9990	0.242	0.223	1.75	7
		0.9966	0.213	0.221	1.54	7
		0.9924	0.229	0.217	1.65	7
		0.9862	0.253	0.211	1.83	6
		0.9778	0.320	0.204	2.31	5
		0.9670	0.376	0.195	2.72	4
		0.9540	0.419	0.183	3.03	4
		0.9387	0.455	0.170	3.28	4

<sup>a</sup> Laboratory momentum of the incident beam.

<sup>b</sup> Total energy in the c.m. system.

<sup>c</sup> The errors quoted are statistical only, corresponding to one standard deviation.

#### IV. INTERPRETATION OF RESULTS

##### A. Theory

As is well known, the differential cross section for spin-0 pions elastically scattering off of unpolarized spin- $\frac{1}{2}$  nucleons can be parameterized as follows<sup>20</sup>:

$$\begin{aligned} \frac{d\sigma}{d\Omega} &= |\text{non-spin-flip amplitude}|^2 \\ &\quad + |\text{spin-flip amplitude}|^2 \\ &= |f|^2 + |g|^2. \end{aligned} \quad (4.1)$$

The amplitudes  $f$  and  $g$  can be expanded into partial-wave amplitudes that represent pion-nucleon states defined by unique values of orbital angular momentum, total angular momentum, and isospin. This expansion can be written

$$\begin{aligned} f(E, \theta) &= \lambda \sum_T \sum_{l=0}^{l_{\text{max}}} [(l+1)a_l A(E)_{l, l^+} + l a_l A(E)_{l, l^-}] \\ &\quad \times P_l(\cos\theta), \end{aligned} \quad (4.2)$$

$$g(E, \theta) = i\lambda \sum_I \sum_{l=0}^{l_{\max}} [a_I A(E)_{I,l^+} - a_I A(E)_{I,l^-}] \times P_l^1(\cos\theta), \quad (4.3)$$

where  $\lambda$  is the center-of-mass wavelength,  $l$  is the orbital angular momentum quantum number,  $l^\pm$  is the total angular momentum quantum number,  $I$  is the isospin quantum number,  $A(E)_{I,l^\pm}$  is the energy-dependent partial-wave scattering amplitude,  $a_I$  is the isospin Clebsch-Gordan coefficient,  $\theta$  is the scattering angle in the center-of-mass reference frame,  $P_l(\cos\theta)$  is the Legendre polynomial of order  $l$ , and  $P_l^1(\cos\theta)$  is the associated Legendre polynomial.

During the past few years several groups have done phase-shift calculations to determine the number of resonances present and their corresponding quantum numbers. These calculations are done by fitting the data using scattering amplitudes that are functions of energy-dependent phase shifts,  $\delta(E)$ , and absorption parameters,  $\eta(E)$ . For simplicity the indices  $I$ ,  $l^\pm$  are dropped from these partial-wave amplitudes, which then have the form

$$A = [\eta \exp(2i\delta) - 1]/2i. \quad (4.4)$$

Phase-shift calculations use the above parameterization or variations of it to fit the data, allowing the  $\delta$ 's,  $\eta$ 's, and  $l_{\max}$  to vary in order to get the best fit. Model-dependent constraints on the  $\delta$ 's and  $\eta$ 's are sometimes employed by the different groups in order to reduce the over-all number of free parameters.

One way of "observing" a resonance is to see if a partial-wave amplitude traces out a counter-clockwise path in the complex plane with increasing energy in such a way that the path crosses or almost crosses the imaginary axis. Once the existence of a resonance is established, a useful expression for the resonant partial-wave amplitude is the Breit-Wigner form given by

$$A_R = \gamma [2(M - E) - i\Gamma]^{-1}, \quad (4.5)$$

where  $\gamma$  is a normalization parameter for a Lorentzian distribution  $[2(M - E) - i\Gamma]^{-1}$  having a mean equal to  $M$  and a full width at half-maximum equal to  $\Gamma$ . The physical interpretation of these parameters is that  $M$  is the mass of the resonance,  $\Gamma$  is the uncertainty in  $M$  and is related to the lifetime of the resonance via the Heisenberg uncertainty principle,  $\tau \approx \hbar/\Gamma$ , and  $\gamma/\Gamma$  equals the elasticity, the fraction of all decays that are elastic. The elasticity is bounded between zero and unity.

A different method of parameterization used to describe pion-nucleon scattering is the direct-channel resonance model.<sup>21</sup> This model assumes

that the differential cross section can be described by partial-wave amplitudes which are the sum of a forward diffraction term,  $f_D, g_D$ , and a resonant term,  $f_R, g_R$ , and are given by the following approximations:

$$f(E, \theta) \approx f_D(E, \theta) + f_R(E, \theta), \quad (4.6)$$

$$g(E, \theta) \approx g_D(E, \theta) + g_R(E, \theta), \quad (4.7)$$

where it is assumed that  $f_D$  goes to zero for large scattering angles and  $g_D$  is identically equal to zero for all angles. This assumption relates the resonant partial-wave amplitudes directly to backward-scattering differential cross sections. Since  $g_D$  is identically equal to zero and  $f_D$  goes to zero at  $180^\circ$ , large-angle elastic scattering provides a sensitive method of observing resonant structure and for determining the parameters of the resonances present.

## B. Discussion

Prior to 1971, there were at least ten phase-shift solutions yielding ten sets of  $\delta$ 's and  $\eta$ 's.<sup>22, 23</sup> The data from this experiment were not available for these solutions. These solutions were employed, therefore, to calculate the cross sections in the angular and momentum range of this experiment. The over-all predictions of these phase-shift solutions did not agree with this experiment. A comparison of a representative selection of these phase-shift predictions with this experiment was discussed by Crabb *et al.*<sup>24</sup>

In 1971 a new phase-shift solution was performed by Almeded and Lovelace (CERN 71).<sup>1</sup> Only the results from this solution will be discussed in detail, since it is the most recent and had more data available for use, including the data of this experiment.

The data of Abillon *et al.*<sup>3</sup> and Rothschild *et al.*<sup>2</sup> were also available for the CERN 71 analysis. Since there was some disagreement among this experiment and the other two, not all the data from the three experiments were included in the solution. It is stated in Ref. 1 that at those momenta and angles where disagreement existed between this experiment and either of the other two, the results of this experiment were used but not those of the disagreeing experiment. This was done because the present experiment was judged to be most consistent and in general had the best over-all agreement with other results. Consequently, the over-all fit of this solution is in good agreement with the data from this experiment. Figure 8 shows the results of the CERN 71 analysis compared to the data of this experiment and the data given in Refs. 3, 4, and 25-30.

The differences between the data of this experi-

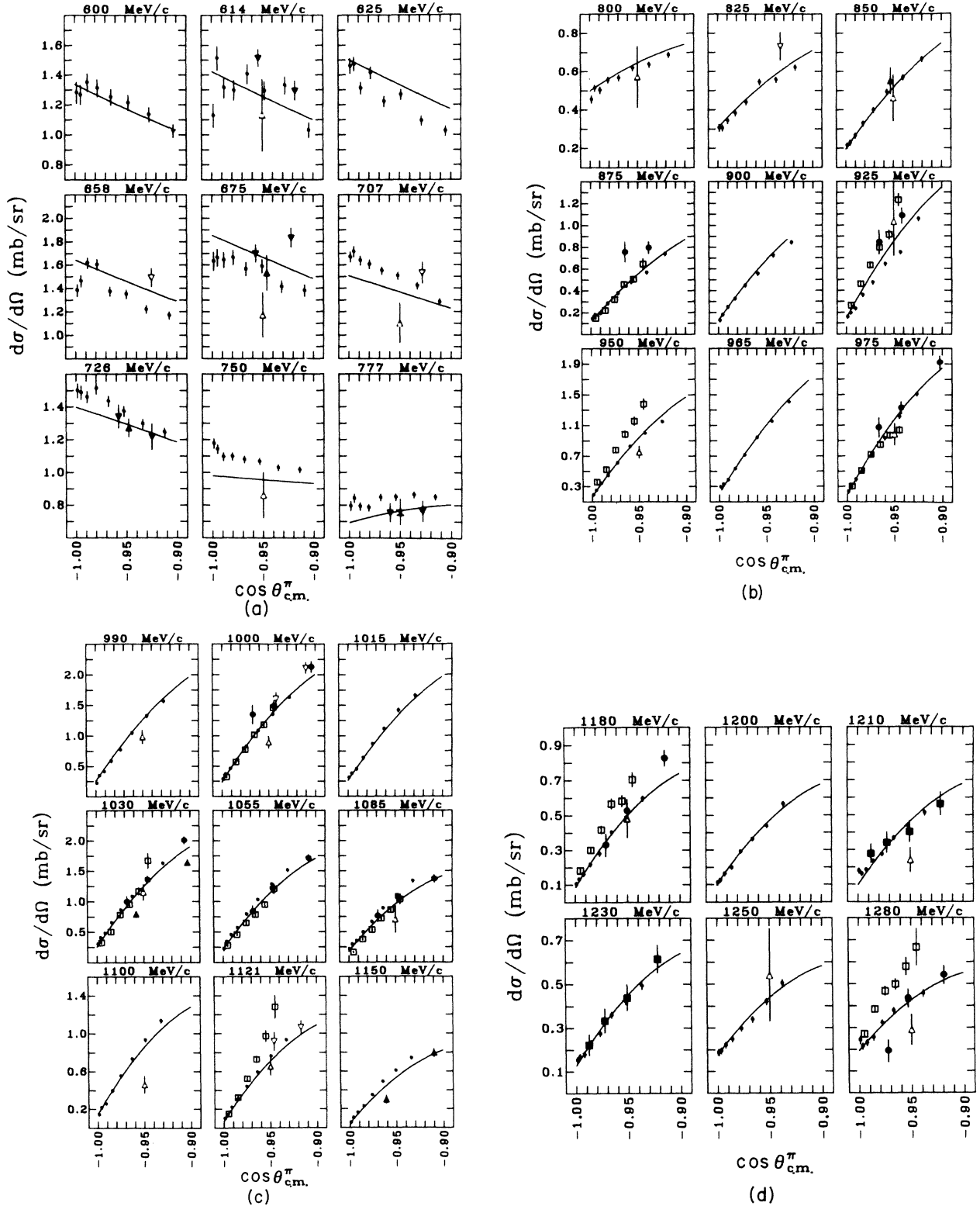


FIG. 8. Negative pion-proton elastic scattering angular distributions for incident pion momenta 600 to 1280 MeV/c. The smooth curves are from the CERN 71 phase-shift solution. The data points correspond to the different experiments as follows:  $\square$ , Ref. 3;  $\blacksquare$ , Ref. 26;  $\triangle$ , Ref. 4;  $\blacktriangle$ , Ref. 27;  $\nabla$ , Ref. 28;  $\blacktriangledown$ , Ref. 29;  $\times$ , Ref. 30;  $\bullet$ , Ref. 31;  $\bullet$ , this experiment.

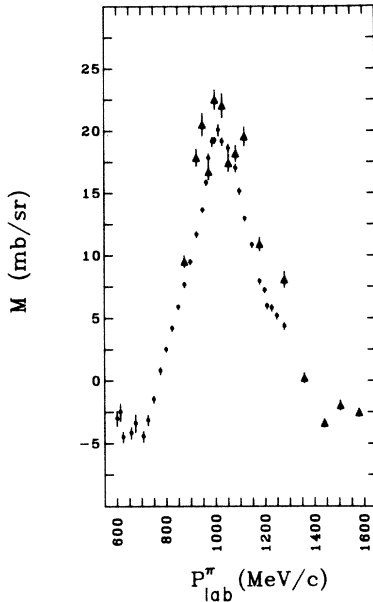


FIG. 9. Angular distributions for Abillon *et al.* (Ref. 3) and this experiment were fitted with a straight line in order to calculate an average slope that is independent of angle. The slope  $M$  of the fitted straight line, where  $M = dy/d\cos\theta$  with  $y = d\sigma/d\Omega$ , is plotted against incident pion momenta in the laboratory. The data points for Abillon *et al.* are denoted by  $\blacktriangle$ , and the data points for this experiment are denoted by  $\bullet$ .

ment and those of Abillon *et al.* is most evident at 925, 950, 1121, 1180, and 1280 MeV/c. For those values of the above momenta where data from other experiments do exist, the agreement between those data and the data from this experiment is better than with the data of Abillon *et al.* The differences at the momentum values listed increase with decreasing scattering angle. This suggests that the differences are not due to an over-all normalization uncertainty at some values of momentum, but are instead due to differences in the backward slope of the angular distributions. In order to examine these differences in slope more quantitatively, an average slope  $M$  was calculated by fitting a straight line to the angular distributions of both sets of data at each momentum.  $M$  is defined as  $dy/d\cos\theta$ , where  $y = d\sigma/d\Omega$  and refers to the fitted straight line. The various values of  $M$  were then plotted as a function of momentum and are shown in Fig. 9. In Fig. 9 the differences in the angular distributions at 925, 950, 1121, 1180, and 1280 MeV/c are reflected in the large differences in the slopes. The average slopes for the data of this experiment form a smooth continuous curve as a function of momentum. This is to be contrasted with the average slopes for the data of Abillon *et al.*, which are not smoothly varying but show a discontinuous behavior and fluctuate as a

function of momentum. This seems to indicate a greater internal consistency for the present experiment.

In the momentum region 670–780 MeV/c the fits of the CERN 71 solution do not agree well with the data of this experiment. In this momentum region the sign of the backward slope of the angular distributions changes from negative to positive, and the magnitude of the cross section falls by more than a factor of 2. This change of sign in the slope is shown clearly in Fig. 9. This disagreement could be the result of insufficient data in this region being included in the solution. The CERN 71 solution, however, fits data at five energy values between 700 and 800 MeV/c; thus, the reason for the poor fit is not clear.

### C. $180^\circ$ differential cross sections

At  $180^\circ$  the spin-flip term in Eq. (4.1),  $g(E, \theta)$ , goes to zero, and the Legendre polynomials reduce to  $(-1)^l$ . The differential cross sections then can be calculated using only  $f(E, \theta)$ :

$$\frac{d\sigma}{d\Omega}(180^\circ) = |f|^2. \quad (4.8)$$

Thus,  $180^\circ$  cross sections make it possible to study the non-spin-flip contributions independently.

Since the largest angle at which data were taken was approximately  $177^\circ$  in the c.m. system, it was necessary to extrapolate to determine the cross sections at  $180^\circ$ . Each of the 33 eight-point angular distributions was fitted with a quadratic polynomial in  $\cos\theta_{c.m.}$ :

$$\frac{d\sigma}{d\Omega_i} = a_{i0} + a_{i1} \cos\theta_{c.m.} + a_{i2} \cos^2\theta_{c.m.}, \quad (4.9)$$

where  $i$  is the index corresponding to values of incident pion momentum,  $i = 1$  to 33.

A least-squares fitting program<sup>31</sup> was used to calculate the coefficients  $a_{ij}$  and their uncertainties which reflected the uncertainties in the data points. The uncertainty in the  $180^\circ$  cross section was obtained from the error matrix calculated by the program and the standard rules for propagation of error. A quadratic form was used to fit the data because it gave values of the reduced  $\chi^2$  which were smaller than the values calculated from linear or cubic fits to the data. No physical significance is attached to the values of the coefficients  $a_{ij}$ . Table III lists the extrapolated cross sections and their corresponding uncertainties.

Abillon *et al.* also extrapolated to  $180^\circ$  using quadratic fits to their data, but they used only data points close to  $180^\circ$ , while Rothschild *et al.* measured the  $180^\circ$  differential cross section directly. Figure 10 shows a comparison of the three experi-

TABLE III. Extrapolated elastic differential cross sections at  $180^\circ$ .

$P_{\text{lab}}$ (MeV/c)	$d\sigma/d\Omega$ (mb/sr)	$u$ [(GeV/c) $^2$ ]	$d\sigma/du$ [mb/(GeV/c) $^2$ ]	Error (%)
600	1.303	0.360	26.55	4
614	1.252	0.357	24.67	5
625	1.451	0.353	27.85	3
658	1.524	0.343	27.15	3
675	1.666	0.338	28.63	3
707	1.683	0.329	27.05	2
726	1.509	0.324	23.36	2
750	1.150	0.318	17.00	2
777	0.790	0.312	11.18	3
800	0.474	0.306	6.41	3
825	0.278	0.300	3.61	5
850	0.197	0.295	2.44	5
875	0.129	0.290	1.54	8
900	0.118	0.284	1.36	9
925	0.143	0.279	1.59	7
950	0.160	0.275	1.71	6
965	0.246	0.272	2.57	4
975	0.209	0.270	2.15	8
990	0.212	0.267	2.15	7
1000	0.257	0.265	2.57	4
1015	0.262	0.263	2.56	7
1030	0.284	0.260	2.72	5
1055	0.225	0.256	2.09	8
1085	0.190	0.251	1.70	7
1100	0.128	0.249	1.12	8
1121	0.081	0.246	0.69	10
1150	0.042	0.241	0.35	20
1180	0.092	0.237	0.74	10
1200	0.098	0.234	0.77	9
1210	0.144	0.233	1.12	7
1230	0.138	0.230	1.04	7
1250	0.181	0.227	1.35	6
1280	0.200	0.224	1.45	6

ments. All three experiments observe the same general structure in the  $180^\circ$  cross section. It falls from a maximum at  $\approx 700$  MeV/c to a first minimum at  $\approx 900$  MeV/c. This first minimum is followed by a rise and turnover that falls to a second minimum at  $\approx 1150$  MeV/c that is lower than the first. The cross section then continues to rise past 1300 MeV/c.

The agreement between these experiments at  $180^\circ$  could be improved greatly if the momentum values of Rothschild *et al.* were increased by 3%. An unknown normalization error in the determination of the momentum for one or more of these experiments would be a possible explanation for this difference. All three experiments claim momentum uncertainties less than 3% differences observed. It must be remembered, however, that the values of Abillon *et al.* and this experiment are extrapolated values.

Since the extrapolations to  $180^\circ$  of Abillon *et al.* and this experiment were made using quadratic

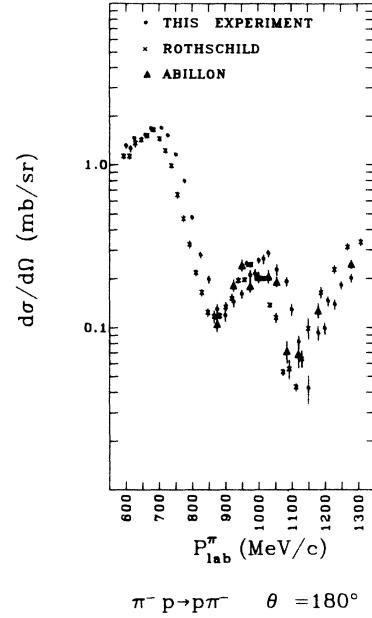


FIG. 10. Negative pion-proton elastic differential cross sections at  $180^\circ$ . The data points correspond to the experiments of Rothschild *et al.* ( $\times$ , Ref. 2), Abillon *et al.* ( $\blacktriangle$ , Ref. 3, extrapolated from  $175^\circ$ ), and this experiment ( $\bullet$ , extrapolated from  $177^\circ$ ).

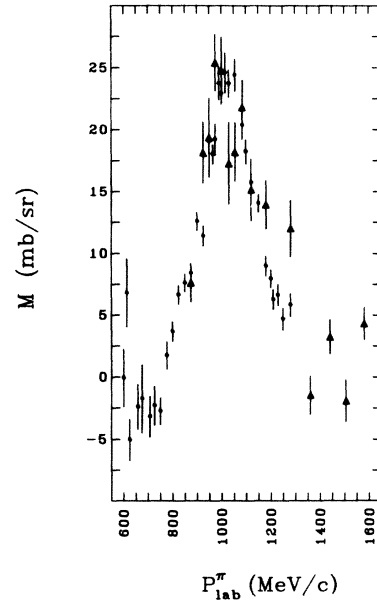


FIG. 11. Slope,  $M$ , of elastic negative pion-proton differential cross sections at  $180^\circ$ . The slopes are extrapolated values that were calculated from quadratic fits to the data of Abillon *et al.* ( $\blacktriangle$ , Ref. 3), and this experiment ( $\bullet$ ).

fits, it is of some interest to use these fits to also calculate the extrapolated slopes at  $180^\circ$ . The slopes at  $180^\circ$  obtained in this way are plotted as a function of momentum in Fig. 11. The over-all shape of the curve is similar to the curve obtained using average slopes shown in Fig. 9. The agreement with Abillon *et al.* is improved over the agreement between the average slopes. This points out again that the differences between the two sets of data are angle-dependent.

In addition to comparing the  $180^\circ$  cross sections from the three experiments, a comparison was also made between the  $180^\circ$  cross sections of this experiment and the CERN 71 solution. The CERN 71 solution fits the extrapolated values of this experiment very well. This is not surprising since the present data were part of the input to the CERN 71 phase-shift analysis. Figure 12 shows the phase-shift solution and the extrapolated cross sections at  $180^\circ$ .

#### D. Direct channel resonance model

In the theory subsection (Sec. IV A) the assumption that only resonant amplitudes were contributing to the elastic differential cross section at large angles was used to relate the resonance parameters directly to the elastic scattering data. At  $180^\circ$  the relationship between the cross sections and the resonant amplitudes simplifies further, because the spin-flip amplitudes vanish. In order to examine this assumption, the  $180^\circ$  cross sections

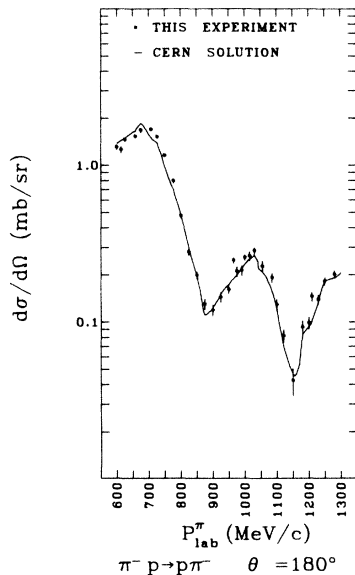


FIG. 12. Negative pion-proton elastic differential cross sections at  $180^\circ$ . The smooth curve is from the CERN 71 phase-shift solution, and the data points are from this experiment, extrapolated from  $177^\circ$ .

were calculated using the resonance parameters from the CERN 71 solution. The differential cross section can be calculated by using Eq. (4.1) and by setting  $g$  equal to zero. The non-spin-flip amplitude,  $f$ , is then expressed in terms of only the resonant partial-wave amplitudes:

$$f = \sum_{k=1}^{23} a_k A_k, \quad (4.10)$$

where  $A_k$  are the resonating partial-wave amplitudes and the  $a_k$  are the products of the isospin Clebsch-Gordan coefficients, angular momentum coefficients, and the Legendre polynomials evaluated at  $180^\circ$ . The resonant partial-wave amplitudes were given the Breit-Wigner form defined by Eq. (4.5).

The CERN 71 resonant parameters<sup>1</sup> were used in Eq. (4.10) for resonating partial-wave amplitudes to calculate the smooth curve shown in Fig. 13. The values of these parameters fit the  $180^\circ$  cross sections poorly. However, these values of resonance parameters are approximate only and contain uncertainties that are not negligible. It was felt that by allowing some of the resonance parameters to vary, a better fit could be obtained. A new set of resonance parameters was determined with the aid of nonlinear fitting procedure<sup>31</sup> which minimized the  $\chi^2$ . The new resonance parameters which are listed in Table IV greatly improve the

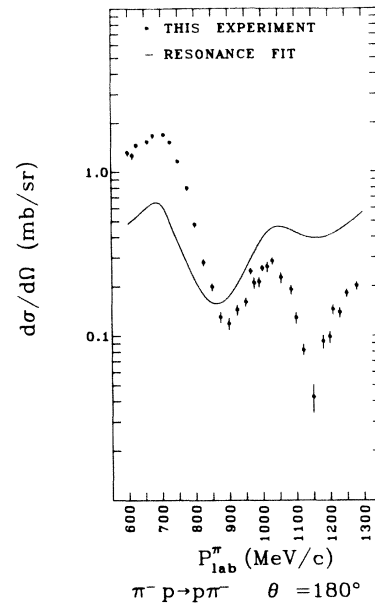


FIG. 13. Negative pion-proton elastic differential cross sections at  $180^\circ$ . The smooth curve is the calculated cross section using only resonant partial waves and the CERN 71 phase-shift-solution values of resonance parameters. The data points are from this experiment, extrapolated from  $177^\circ$ .

TABLE IV. Resonance parameters determined from a least-squares fit to the  $180^\circ$  extrapolated elastic differential cross sections.

Resonant wave $L_{2I,2J}$	Mass (MeV)	$\Gamma$ (MeV)	$\gamma/\Gamma$
$S_{31}$	1690	165	0.29
$P_{31}$	1919	296	0.14
$P_{33}$	1235	129	1.00
$P_{33}$	1663	221	0.08
$P_{33}$	2163	186	0.34
$D_{33}$	1722	236	0.19
$D_{35}$	2185	592	0.27
$F_{35}$	1871	231	0.20
$F_{37}$	1963	153	0.53
$S_{11}$	1501	64	0.19
$S_{11}$	1657	102	0.74
$S_{11}$	2089	188	0.46
$P_{11}$	1437	213	0.43
$P_{11}$	1762	371	0.11
$P_{13}$	1867	315	0.21
$D_{13}$	1516	106	0.69
$D_{13}$	2076	140	0.33
$D_{15}$	1683	165	0.41
$D_{15}$	2085	132	0.27
$F_{15}$	1688	136	0.67
$F_{15}$	2184	178	0.17
$F_{17}$	2031	168	0.07
$G_{17}$	2207	143	0.43

fit to the  $180^\circ$  cross sections of this experiment, as can be seen in Fig. 14.

A meaningful comparison of the new values of the parameters with the CERN 71 values is difficult since the uncertainties in both sets of parameters are not known. All of the resonant masses for the improved fit agree with the CERN 71 solution to within a few percent. The new values of resonance widths agree with the CERN 71 values to within 20% except for the widths of  $P_{31}(1900)$ ,  $F_{37}(1925)$ ,  $S_{11}(1500)$ , and  $P_{11}(1720)$ . Although these widths differ by more than 20% from the CERN 71 solution, they lie within the range of values found in earlier solutions.<sup>22</sup> The biggest disagreements with the CERN 71 parameters occur in the values of the  $\gamma$ 's, the partial widths. Six of the 23 partial widths differed by more than 20%. Of these six, all lie within the range of values of the previous solutions except the  $\gamma$ 's for  $P_{31}(1900)$  and  $F_{17}(2000)$ . The small values of  $\gamma$  for these two resonances give lower values of elasticities than found by other phase-shift solutions.

The fit in Fig. 14 is good except for the dip region at 1150 MeV/c. The main reason for doing the fit, however, was not to determine a unique set of resonance parameters that fit these data, but to show that a set of resonance parameter values consistent with the values found by others

exists and provides a good description of the  $180^\circ$  cross section. The ability to fit the  $180^\circ$  cross section using only resonant partial-wave amplitudes gives only resonant support to the assumption of Wrighton *et al.*<sup>21</sup> that at large angles the background or diffraction contribution to the cross sections is negligible in this momentum region.

## V. CONCLUSIONS

This experiment provides a systematic set of data for  $\pi^-p$  elastic scattering in the momentum region where pion-nucleon interactions are described in terms of resonances. Few data existed at large angles for  $\pi^-p$  elastic scattering prior to this experiment. The discussion of these data in relation to other work, both experimental and phenomenological, leads to the following conclusions.

(a) The data of this experiment are in agreement with previous data except for the data of Abillon *et al.*<sup>3</sup> at 925, 950, 1121, 1180, and 1280 MeV/c. These differences have been traced to the discontinuous momentum dependence in the background slope of the angular distributions for the data of Abillon *et al.*

(b) The extrapolated  $180^\circ$  cross sections show the same structure as the  $180^\circ$  measurements of Rothschild *et al.*<sup>2</sup> except that the two sets of cross sections are different with respect to momentum.

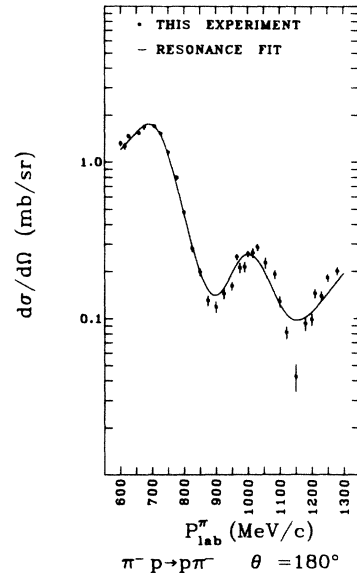


FIG. 14. Negative pion-proton elastic differential cross sections at  $180^\circ$ . The smooth curve is calculated from a least-squares fit to the data using only resonant partial waves and adjusted resonance parameters. CERN 71 resonance parameters were used for the initial guess, and the data points are from this experiment, extrapolated from  $177^\circ$ .

A 3% momentum shift in either set would greatly improve the agreement. This difference may also be dependent on the extrapolation procedure employed.

(c) The CERN 71 phase-shift solution fits the data of this experiment well except in the momentum region 670–780 MeV/c. In this region the sign of the slope of the angular distributions goes from negative to positive.

(d) The data of this experiment were used to calculate the differential cross sections at  $180^\circ$ . A good fit to these extrapolated cross sections was obtained by using only resonating partial-wave amplitudes. The values of resonance parameters

for the fit differed by less than 20% from the values of resonance parameters found by the CERN 71 solution or by previous solutions except for four values of the partial widths. This supports the direct-channel resonance model of Wrighton *et al.*<sup>21</sup> that assumes only resonant contributions to the differential cross sections at large scattering angles.

#### ACKNOWLEDGMENTS

The authors are grateful to the entire Bevatron staff for their invaluable support, assistance, and encouragement throughout the experiment.

\*Work supported in part by the Ames Laboratory of the U. S. Atomic Energy Commission and the National Research Council of Canada.

†This work is based in part on the dissertation submitted by T. J. Richards to the Graduate School of Saint Louis University in partial fulfillment of the requirements for the Ph.D. degree.

‡Present address: Research Department, Caterpillar Tractor Company, Peoria, Illinois 61602.

§Present address: Nuclear Physics Laboratory, Oxford University, Oxford, England.

|| Present address: Virginia Polytechnic Institute, Blacksburg, Virginia 24061.

\*\*Present address: Rutherford Laboratory, Chilton, Didcot, Berkshire, England.

†† Present address: TRIUMF, University of British Columbia, Vancouver, British Columbia, Canada.

‡‡ Present address: Lawrence Berkeley Laboratory, Berkeley, California 94720.

<sup>1</sup>S. Almehed and C. Lovelace, CERN report 1971 (unpublished); Nucl. Phys. **B40**, 157 (1972).

<sup>2</sup>R. E. Rothschild, T. Bowen, P. D. Caldwell, D. Davidson, E. W. Jenkins, R. M. Kalbach, D. V. Peterson, and A. E. Pifer, Phys. Rev. D **5**, 499 (1972).

<sup>3</sup>J. M. Abillon, A. Borg, M. Crozon, T. Leray, J. P. Mendiburu, and J. Tocqueville, Phys. Lett. **32B**, 712 (1970).

<sup>4</sup>A. D. Brody, R. J. Cashmore, A. Kernan, D. W. G. S. Leith, B. S. Levi, B. C. Shen, J. P. Berge, D. J. Herndon, R. Longacre, L. R. Price, A. H. Rosenfeld, and P. Söding, Phys. Rev. D **3**, 2619 (1971); SLAC Report No. SLAC-PUB-789, Suppl. 1, 1970 (unpublished).

<sup>5</sup>T. J. Devlin, UCRL Report No. UCRL 9727, 1961 (unpublished).

<sup>6</sup>J. E. Jensen, R. B. Stewart, and W. A. Tuttle, editors, Brookhaven National Laboratory report (unpublished).

<sup>7</sup>F. James, CERN Computer Library No. W505, 1968 (unpublished).

<sup>8</sup>T. J. Richards, Ph.D. thesis, Saint Louis University, 1972 (unpublished).

<sup>9</sup>N. Abbattista, M. Biasco, S. Mongelli, A. Romano, P. Waloschek, and E. Perez-Ferreira, Nuovo Cimento **23**, 1 (1962).

<sup>10</sup>C. J. Batty, Proc. Phys. Soc. **76**, 577 (1960).

<sup>11</sup>M. J. Longo and B. J. Moyer, Phys. Rev. Lett. **9**, 466 (1962).

<sup>12</sup>R. H. Miller, Nuovo Cimento **6**, 882 (1957).

<sup>13</sup>T. A. Fujii, Phys. Rev. **113**, 695 (1959).

<sup>14</sup>H. Palevsky, T. L. Friedes, R. J. Sutter, G. W. Bennett, G. J. Igo, W. D. Simpson, G. C. Phillips, D. M. Corley, N. W. Wall, R. L. Stearns, and B. Gottschalk, Phys. Rev. Lett. **18**, 1200 (1967).

<sup>15</sup>M. J. Longo and B. J. Moyer, Phys. Rev. **125**, 701 (1962).

<sup>16</sup>T. Bowen, M. Di Corato, W. H. Moore, and G. Tagliaferri, Nuovo Cimento **9**, 908 (1958).

<sup>17</sup>L. S. Azhgirey, Yu. P. Kumekin, M. G. Mescheryakov, S. B. Nurusev, G. D. Stoletov, and Huang De-Tsang, Nucl. Phys. **43**, 213 (1963).

<sup>18</sup>E. Lillenthun, Phys. Rev. **125**, 665 (1962).

<sup>19</sup>C. J. Batty, Nucl. Phys. **23**, 562 (1961).

<sup>20</sup>R. J. Cence, *Pion-Nucleon Scattering* (Princeton Univ. Press, Princeton, New Jersey, 1969).

<sup>21</sup>G. C. Wrighton, W. A. Ross, and D. W. G. S. Leith (unpublished). We thank W. A. Ross at McGill University for a copy of this work.

<sup>22</sup>D. J. Herndon, A. Barbaro-Galtieri, and A. H. Rosenfeld, UCRL Report No. UCRL 20030, 1970 (unpublished).

<sup>23</sup>The three Berkeley solutions are no longer used because of programming errors. We thank J. Zoba, Particle Data Group, Lawrence Berkeley Laboratory, for bringing this to our attention.

<sup>24</sup>D. G. Crabb, R. Keller, J. R. O'Fallon, T. J. Richards, R. J. Ott, J. Trischuk, J. Va'vra, and L. S. Schroeder, Phys. Rev. Lett. **27**, 216 (1971).

<sup>25</sup>P. S. Aplin, I. M. Cowan, W. M. Gibson, R. S. Gilmore, K. Green, J. Malos, V. J. Smith, D. L. Ward, M. A. R. Kemp, A. T. Lea, R. McKenzie, and G. C. Oades, Nucl. Phys. **B32**, 253 (1971).

<sup>26</sup>C. D. Wood, T. J. Devlin, J. A. Helland, M. J. Longo, B. J. Moyer, and V. Perez-Mendez, Phys. Rev. Lett. **6**, 481 (1961).

<sup>27</sup>J. A. Helland, C. D. Wood, T. J. Devlin, D. E. Hagge, M. J. Longo, B. J. Moyer, and V. Perez-Mendez, Phys. Rev. **134**, B1079 (1964).

<sup>28</sup>P. M. Ogden, D. E. Hagge, J. E. Helland, M. Banner, J. Detoef, and J. Teiger, Phys. Rev. **137**, B1115 (1965).

- <sup>29</sup>J. D. Oliver, J. Nadelhaft, and G. B. Yodh, Phys. Rev. 147, 932 (1966).
- <sup>30</sup>P. J. Duke, D. P. Jones, M. A. R. Kemp, P. G. Murphy, J. D. Prentice, and J. J. Thresher, Phys. Rev. 149, 1077 (1966).

- <sup>31</sup>P. R. Bevington, *Data Reduction and Error Analysis For the Physical Sciences* (McGraw-Hill, New York, 1969). Program LEGFIT was used for linear fitting functions and CURFIT was modified and used for nonlinear fitting functions.